Conference on Modelling Fluid Flow (CMFF'25)
The 19th International Conference on Fluid Flow Technologies
Budapest, Hungary, August 26 - August 29, 2025

EVALUATING THE PROBABILITY OF INFECTION IN A UK HOSPICE THROUGH A CFD DRIVEN METRIC

Mohammad ELSARRAJ[1], Yasser LARIMI[2], Amir KESHMIRI[3]

[1] Corresponding Author: Department of Fluids & Environment, School of Engineering, The University of Manchester, Manchester, M13 9PL, UK. E-mail: mohammad.elsarraj@manchester.ac.uk
[2] Department of Fluids & Environment, School of Engineering, The University of Manchester, Manchester, M13 9PL, UK.
[3] Department of Fluids & Environment, School of Engineering, The University of Manchester, Manchester, M13 9PL, UK.

ABSTRACT

Hospices house vulnerable patients with severely weakened immune systems, making control of airborne virus transmission critical. This study introduces a Probability of Infection (POI) metric, quantified through Computational Fluid Dynamics (CFD) using a transient Eulerian-Lagrangian (E-L) model to simulate airborne particle transport and exposure. Simulations include exhaled CO_2 and infectious aerosols to explore spatial correlations, revealing that while CO_2 and POI distributions exhibit similarities, they diverge due to differences in diffusion behaviour. Across 13 scenarios, POI heatmaps identify high-risk zones influenced by airflow patterns and infector position, not solely by CO_2 levels. The findings highlight the limitations of relying on CO_2 concentration as a proxy for infection risk and demonstrate the value of direct aerosol modelling in assessing ventilation effectiveness. This approach offers a robust basis for improving infection risk evaluation in sensitive indoor healthcare environments.

Keywords: Finite Volume Method, Indoor Air Quality, Indoor Virus Transmission, CFD, Fluid Dynamics

Nomenclature

C_d	Drag coefficient
P	Pressure [pa]
Pr	Prandtl number
Re_d	Reynolds number of particle
T	Mean temperature [K]
U_i	Mean velocity component in Cartesian
Greek Symbols	
μ	Dynamic viscosity [Pa s]
ρ	Density [kg/m^3]
Acronyms	
E-L	Eulerian-Lagrangian model
IR	Infection risk
POI	Probability of infection (%)

Additional symbols and acronyms are defined in the text.

1. INTRODUCTION

The risk of infectious particle transport via ventilation systems has gained significant attention, particularly during the COVID-19 pandemic [1–4]. Virus transmission is especially efficient in enclosed, crowded indoor environments such as offices, restaurants, and public transport [5]. Ventilation plays a crucial role in mitigating airborne transmission by removing indoor pollutants and replacing contaminated air. Consequently, organisations such as the Chartered Institution of Building Services Engineers (CIBSE), the American Society of Heating, Refrigerating and Air-Conditioning Engineers (ASHRAE) and the Federation of European Heating, Ventilation and Air Conditioning Associations (REHVA) have issued guidelines advocating increased outdoor air exchange to reduce airborne pathogen exposure [6–8]. However, the optimal ventilation rate required to mitigate airborne contagion remains unclear [9]. Moreover, a trade-off exists: while ventilation dilutes contaminants, it may also contribute to aerosol dispersion, potentially increasing infection risk [10]. This study seeks to establish an optimal balance by refining ventilation strategies for infection risk mitigation.

Traditionally, infection risk has been assessed through airborne pollutant concentration metrics. Several studies have utilised computational fluid dynamics (CFD) simulations to evaluate ventilation strategies and their impact on airborne particle dispersion [9,11,12]. Research has explored natural and mechanical ventilation designs, air distribution patterns, and physical barriers to control droplet transmission in settings such as classrooms, office spaces, and aircraft cabins[13,14]. However, these studies primarily focus on particle presence and concentration, often overlooking critical transmission parameters such as exposure duration, viral load, and individual susceptibility.

To address these limitations, this study introduces a novel infection risk probability metric based on a transient Eulerian-Lagrangian CFD approach. The metric quantifies long-range airborne transmission by incorporating spatial-temporal particle concentration, exposure time, and clinical viral load data. This allows for a more realistic assessment of cumulative viral exposure over time, which is essential for understanding transmission risk in shared indoor environments. Given that human respiratory activities (e.g., breathing, speaking, coughing) generate droplets ranging from 0.01 to 1000 μm [15], understanding the behaviour of these aerosols in ventilated spaces is essential.

The CFD model is applied to a hospice communal space and captures airflow variations driven by fluctuating wind pressures on operable windows. By analysing the distribution of infectious aerosols and comparing it to exhaled CO_2 concentrations, the study identifies key differences in dispersion behaviour and highlights the importance of particle-based infection modelling for effective ventilation assessment. The communal space is demonstrated by Figure 1.

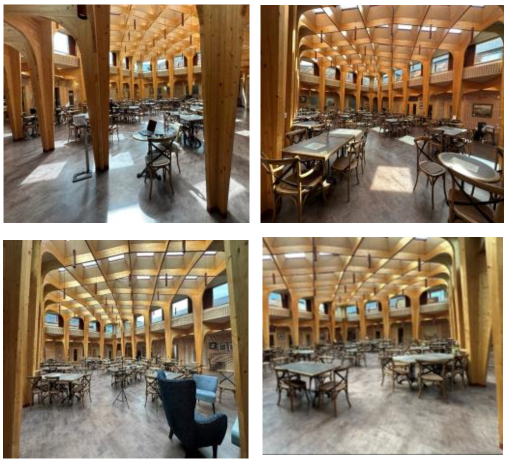

Figure 1. The communal area of the UK Hospice.

2. METHODOLOGY

2.1 The Eulerian-Lagrangian CFD Model

2.1.1 Background

Accurately evaluating airborne infection risk, particularly for COVID-19, requires modelling viral emission, transport, and inhaled exposure over time. Infections may arise from prolonged exposure to low concentrations of virus-laden aerosols, reinforcing the importance of spatial and temporal resolution in dose estimation. The Lagrangian approach is well-established in indoor air quality research for tracking aerosolised particles. It resolves forces such as drag, gravity, and turbulent dispersion, allowing accurate characterisation of airborne transport and deposition patterns and quantifying viral dose [13,14].

This study employs the **Eulerian-Lagrangian CFD approach** based on Crowe et al. [16], modelling air (continuous phase) via Eulerian equations while tracking particles (dispersed phase) with a transient Lagrangian method. The model simulates infectious particle transport during speech, outputting particle volume, count, and fraction per computational cell. This data, combined with clinical inputs, enables spatial-temporal infection probability estimation.

2.1.2 The Eulerian Model

As the governing equations for the mass, momentum, and energy equations, Navier-Stokes is used to model the unsteady incompressible flow field using an Eulerian approach:

$$\frac{\partial \rho}{\partial \mathrm{t}} + \frac{\partial (\rho \mathrm{U_i})}{\partial \mathrm{x_i}} = 0 \tag{1}$$

$$\frac{\partial (\rho \mathrm{U_i})}{\partial \mathrm{t}} + \frac{\partial}{\partial \mathrm{x_j}}(\rho \mathrm{U_i U_j}) = -\frac{\partial \mathrm{P}}{\partial \mathrm{x_i}} + \frac{\partial}{\partial \mathrm{x_j}}\left(\mu \frac{\partial \mathrm{U_i}}{\partial \mathrm{x_j}} - \rho \overline{\mathrm{u_i u_j}}\right) \tag{2}$$

$$\frac{\partial (\rho T)}{\partial t} + \frac{\partial}{\partial x_j}(\rho U_j T) = \frac{\partial}{\partial x_j}\left(\frac{\mu}{Pr}\frac{\partial T}{\partial x_j} - \rho \overline{u_j \theta}\right) \tag{3}$$

where, ρ is the density and $\overline{\mathrm{u_j}\theta}$ is the turbulent heat flux vector, respectively.

The present authors have previously shown the importance of the choice of the turbulence model on the prediction of fluid flow and heat transfer [17–19]. Consequently, the present authors have also investigated six different types of eddy viscosity models to determine the most feasible in predicting indoor air flow [20]. The φ–f model was chosen for its stability and near-wall performance and the same model will be used in this present study. Since this a low-Reynolds-number turbulence model, the grids were adjusted to be very fine along the wall (the wall-adjacent cell typically extends only to $y^+ \leq 1$), in order for the turbulent boundary layers to be fully resolved.

2.1.3 The Lagrangian Model

The momentum equation for particles is derived from the balance between inertial forces and external forces applied to the particle:

$$m_p \frac{dv_p}{dt} = \frac{m_p(v_c - v_p)}{\tau_r} + m_p g + F \qquad (4)$$

Where, for a spherical particle with a diameter of d_p immersed in continuous air, g is the gravitational force exerted on the particle, F represents additional forces acting on the particle surface, specifically the drag force (C_d), virtual mass force, and pressure gradient **force** all of which were modelled using the standard Lagrangian particle tracking approach implemented in the CFD solver. v_c is the velocity of the continuous phase, v_p is the particle velocity and τ_r is the momentum relaxation time scale computed as:

$$\tau_r = \frac{2m_p}{\rho_c A_p C_d (v_c - v_p)} \qquad (5)$$

where, ρ_c is the density of the continuous phase and A_p is the projected area of the particle. The Drag force (C_d) is modelled through the Schiller-Naumann Correlation [21], which is a function of the particle Reynolds number:

$$Re_d = \frac{\rho_c |v_c - v_p| D_p}{\mu_c} \qquad (6)$$

where, μ_c is the dynamic viscosity of the continuous phase and D_p is the diameter of the particle.

2.1 Infection Risk Metric

2.1.1 The Wells-Riley Model

The Wells–Riley model estimates airborne infection probability (POI) as a function of inhaled quanta (n), defined as the dose causing infection in 63% of susceptible individuals [22,23]. Assuming a uniform aerosol concentration:

$$POI = 1 - e^{-n} = 1 - e^{-(q_c \times IR \times t_e)} \qquad (7)$$

where, q_c is the quanta concentration [quanta/m³], IR is the inhalation rate, and t_e is the exposure time. However, the model assumes well-mixed, steady-state conditions, which rarely hold in indoor spaces with complex airflow and localised sources. This limitation motivates the need for spatially and temporally resolved approaches, as detailed in the following subsection.

2.1.2 Virion Concentration and POI at Each Cell

This study employs a Probability of Infection (POI) metric, incorporating particle count, exposure duration, and clinical data. Using CFD and a time-dependent Eulerian-Lagrangian (E-L) model, the emission and distribution of infectious airborne particles (quanta) are computed.

Initially, the quanta concentration at each computational cell is determined using Eq. (7), where the sum of the particle-to-air volume fraction ($\alpha_{p,cell}$) and the initial hydrated particle volume ($Vol_{i,cell}$) is normalised by the evaporated desiccated volume and multiplied by the viral load c_v, taken as 2.35×10^9 [quanta/mL] [24]. This number is multiplied by 10^6 to convert to quanta/m³.

The total inhaled quanta at each cell, (D_{cell}), is then obtained by integrating the quanta concentration over time, as expressed in Eq. (8). This value is subsequently substituted into the Wells-Riley equation to compute the Probability of Infection (POI) at each cell, using Eq. (9). The resulting POI values generate a spatio-temporal infection risk (IR) map, illustrating areas of elevated exposure risk.

$$q_{c,cell} = c_v \frac{\sum_{j=0}^{t}(\alpha_{p,cell_j} \; Vol_{pi,cell_j})}{Vol_p} \times 10^6 \qquad (7)$$

$$D_{cell} = IR \int_0^T q_{c,cell} \, dt \quad [quanta] \qquad (8)$$

$$POI = \left(1 - e^{(-D_{cell})}\right) \times 100 \, [\%] \qquad (9)$$

2.1.3 Infection Risk Metric and Particle Assumptions

A time-dependent Eulerian–Lagrangian CFD model was used to compute particle transport and quanta concentration at each cell. Concentration was calculated using Eq. (7), combining local particle volume fraction and hydrated droplet volume, scaled by a viral load of $c_v = 2.35 \times 10^9$ quanta/mL and converted to quanta/m³. The inhaled dose was integrated over time (Eq. 8) and used in the Wells–Riley model (Eq. 9) to estimate the POI.

Based on Li et al. [25], the volume-weighted mean diameter of respiratory droplets is 6.62 μm. This study assumes all droplets rapidly dehydrate into aerosols and adopts this diameter as representative of airborne transmission. Dehydrated droplet nuclei are 20–34% smaller due to water loss; Li et al. [25] estimated a final diameter equal to 26.2% of the original, using data from Chao et al.

[26] and Li et al. [27], consistent with Stadnytskyi et al. [28]. Accordingly, a shrinkage factor of 0.262 is applied in volume calculations. Viral decay is neglected to reflect a conservative, worst-case infection scenario. At this size, particle motion is governed by drag, gravity, and turbulence; Brownian diffusion was excluded and is noted as a limitation. Viral load was assumed proportional to droplet volume, as in [37], though finer particles may carry higher concentrations [29].

2.2 CO_2 and Age of Air Numerical Models

Occupant-generated CO_2 emissions are modelled using the species transport equation to compare infection risk (IR) and CO_2 concentration distributions.

The mean ventilation effectiveness in the occupied zone (E_{OZ}) is evaluated using the age of air (θ_{age}) [30], modelled via the passive scalar transport equation. This approach assigns a virtual "clock" to each air volume element, tracking the time elapsed since uncontaminated outdoor air entered a given cell. Consequently, this enables the assessment of air distribution and age across different office space regions.

2.2.1 CO_2 Species Transport Numerical Model

The three-dimensional species transport equation to simulate the transport of CO_2 within the office room is implemented in this study:

$$\frac{\partial(\rho Y_{CO2})}{\partial t} + \frac{\partial(\rho Y_{CO2} U_j)}{\partial x_j} = \frac{\partial}{\partial x_j}\left[\rho D_{CO2}\frac{\partial(Y_{CO2})}{\partial x_j} + \frac{\mu_t}{\sigma_t}\frac{\partial Y_{CO2}}{\partial x_j}\right] \tag{10}$$

where t is the simulation time, ρ is the overall density of the mixture, Y_{CO2} is the mass fraction of CO_2, U_j is the velocity where u_1, u_2, u_3 are the directions in the x, y and z directions respectively, μ_t is the turbulent dynamic viscosity, σ_t is the turbulent Schmidt number and D_{CO2} is the molecular diffusivity of CO_2 in the mixture. The turbulent diffusion is accounted for through the term $\frac{\mu_t}{\sigma_t}$.

The occupants were represented by a box, 0.25 m x 0.4 m x 1.2 m, in the computational model, [31]. The exhaled CO_2 was introduced via a small circular hole of 10-mm at the height of 1.1 m of the box. Table 1 summarises the boundary conditions for the occupant. The peak occupancy is 88 people.

Table 1. Boundary conditions for the occupant CO_2 exhalation for each case.

Activity	CO_2 Exhalation Rate [L/min]	Inlet Type	Heat Source (W)
Sedentary	0.31 [32]	Circular Inlet	75

2.2.2 Age of Air Numerical Model

The age of air is modelled through the passive scalar transport equation:

$$\frac{\partial \rho A}{\partial t} + u_j\frac{\partial \rho A}{\partial x_j} - \frac{\partial}{\partial x_j}\left[D\frac{\partial \rho A}{\partial x_j}\right] - S_A = 0 \tag{11}$$

where A is the passive scalar of the age of air, D is the diffusivity flux of the passive scalar, and S_A is the source term for the age of air, which is a scalar flux with an inferred density of 1/s. The passive scalar's diffusivity characteristics were set by increasing the Schmidt number and the Turbulent Schmidt number to a value of 1×10^9. Consequently, advection can dominate the transport of the time scalar when there is flow motion, whereas diffusion can operate on the scalar when there is little to no advection.

Local and Mean Ventilation Effectiveness

Air Changes per Hour (ACH) quantifies the total volume of air entering a space relative to its internal volume, representing the nominal ventilation rate. However, this metric only accounts for the total fresh air supply without considering its distribution within the space.

To assess air distribution, local ventilation rates are calculated based on the age of air at each cell. This provides a more detailed evaluation of airflow patterns, ensuring a comprehensive understanding of ventilation effectiveness. The age distribution theory, as outlined in [33], forms the basis of this approach:

$$n_{cell} = \frac{1}{A_{cell}} \tag{12}$$

Ventilation effectiveness, denoted as n_{cell}, is determined by comparing the actual delivery rate of outside air with an ideal mixing scenario. In a perfectly mixed environment, where ventilation is uniform and concentrations are equal throughout, the local ventilation efficiency at each cell (E_{cell}) is calculated as:

$$E_{cell} = \frac{n_{cell}}{N} \tag{13}$$

According to ASHRAE [34], the occupied zone, referring to the area where humans occupy, extends up to 1.8 meters from the floor and 0.3 meters from the side walls. To determine the average ventilation effectiveness in this zone (E_{OZ}), we calculate the volume average of the local ventilation effectiveness within this range. This involves summing up products of E_{cell} and cell volumes, then dividing by the total cell volumes in the occupied zone.

2.3 A Description of IES:VE Energy Modelling

The Integrated Environmental Solutions Virtual Environment (IES:VE) is a comprehensive building performance simulation suite used by architects and engineers to optimise energy efficiency and occupant comfort. It has been validated against international standards, including ASHRAE 140 and CIBSE TM33, ensuring compliance with rigorous industry benchmarks [35].

2.4 Cases Studied

Figure 2 shows the computational domain of the hospice dining space. The passive ventilation system includes upper operable windows (red, labelled 1–4) for exhaust and lower intakes (blue, labelled 1–2) for fresh air supply. Internal doors (green, labelled 1–2) are opened under overheating conditions to allow cross-zone airflow. As a passive system, flow direction can reverse depending on wind and pressure, resulting in either positive or negative airflow through the openings.

To capture realistic ventilation-driven airflow conditions throughout the year, hourly data from dynamic simulation was analysed using a custom script. This process identified 13 representative days that collectively span the full range of ventilation performance across all opening types, covering the minimum, maximum, and key quartiles (Q1, Q2, Q3). These selected cases ensure efficient yet comprehensive CFD coverage of both typical and extreme conditions, where openings may act as inlets or exhausts depending on wind-driven pressure differences. These cases are outlined by Table 2 below.

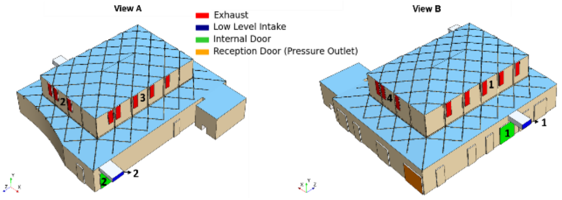

Figure 1. The computational domain of the communal area within the UK hospice used in the present study.

Table 2. Boundary conditions for the occupant CO_2 exhalation for each case.

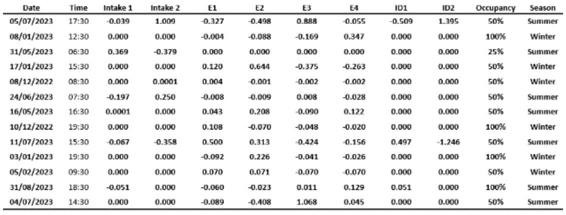

Date	Time	Intake 1	Intake 2	E1	E2	E3	E4	ID1	ID2	Occupancy	Season
05/07/2023	17:30	-0.039	1.009	-0.327	-0.498	0.888	-0.055	-0.509	1.395	50%	Summer
08/01/2023	12:30	0.000	0.000	-0.004	-0.088	-0.169	0.347	0.000	0.000	100%	Winter
31/05/2023	06:30	0.369	-0.379	0.000	0.000	0.000	0.000	0.000	0.000	25%	Summer
17/01/2023	15:30	0.000	0.000	0.120	0.644	-0.375	-0.263	0.000	0.000	50%	Winter
08/12/2022	08:30	0.000	0.0001	0.004	-0.001	-0.002	-0.002	0.000	0.000	50%	Winter
24/06/2023	07:30	-0.197	0.250	-0.008	-0.009	0.008	-0.028	0.000	0.000	50%	Summer
16/05/2023	16:30	0.0001	0.000	0.043	0.208	-0.090	0.122	0.000	0.000	50%	Summer
10/12/2022	19:30	0.000	0.000	0.108	-0.070	-0.048	-0.020	0.000	0.000	100%	Winter
11/07/2023	15:30	-0.067	-0.358	0.500	0.313	-0.424	-0.156	0.497	-1.246	50%	Summer
03/01/2023	19:30	0.000	0.000	-0.092	0.226	-0.041	-0.026	0.000	0.000	100%	Winter
05/02/2023	09:30	0.000	0.000	0.070	0.071	-0.070	-0.070	0.000	0.000	50%	Winter
31/08/2023	18:30	-0.051	0.000	-0.060	-0.023	0.011	0.129	0.051	0.000	100%	Summer
04/07/2023	14:30	0.000	0.000	-0.089	-0.408	1.068	0.045	0.000	0.000	50%	Summer

2.5 Acceptable POI Level

The acceptable POI level, determined to be 7.5% in England based on worst case government statistics, is based on the methodology proposed by the authors in a companion paper [37].

2.6 Lagrangian Particle Injector

The exhaled droplets (dispersed phase) from the infector are simulated using a transient Lagrangian model. This study implements "one-way" coupling between the dispersed phase (airborne particles) and the continuous phase (air-CO_2 mixture). As confirmed in our companion paper [37], the volume fractions of the airborne particles are so insignificant that their displacement of the air-CO_2 mixture is negligible. Consequently, the particle transport is affected only by the fluid motion, without influencing the air flow in return. The overall simulated time was 5 minutes with a droplet time step of 0.01s. This time was sufficient for the IR level to reach the acceptable limit based on worst-case scenarios. The residuals were left to reach a minimum level of 10^{-6} to regulate the particle tracking's accuracy. Table 3 demonstrates the numerical boundary conditions applied for the particle injector.

Table 3. Boundary Conditions for the Lagrangian Particle Injector.

Variable	Value/Type	Reference
Injector Type	Point injector	-
Injection Rate	1000 [particle/s]	[28]
Injection Direction	Normal	-
Particle Diameter	6.62 [µm]	[25]
Activity	Speaking	-
Particle Injection Velocity	4.07 [m/s]	[38]
Particle Temperature	34 [°C]	[39]
Particle Deposition Rate	0.285 [cm/s]	[40]

3. RESULTS

3.1 Distribution and Behavioural Analysis

3.1.1 Contour Plots

Figures 3 & 4 illustrate the Probability of Infection (POI) and CO_2 concentration contours along the horizontal plane (1.2 m above the floor) and vertical mid-span plane. The results indicate that airflow forces significantly influence the distribution of both infectious particles and CO_2, with higher concentrations in recirculation zones and low-velocity regions, where airborne particles tend to accumulate.

While CO_2 concentration and infection risk share distributional similarities, key differences are observed. The CO_2 species transport model exhibits ‘smearing’ effects, where CO_2 disperses more uniformly from high- to low-concentration areas due to diffusion. In contrast, the infection risk formulation lacks a diffusion term, resulting in sharper concentration gradients and more localised risk zones.

Given the extensive number of contour plots across multiple cases, only representative cases are presented. To facilitate a comprehensive comparison across all 13 cases assessed in this study, heatmaps are employed, offering a more insightful and quantitative analysis of POI and CO_2 distribution patterns.

3.1.2 Heatmaps

Figures 5 & 6 show the average Probability of Infection (POI) and CO_2 concentration at 1.2 m above the floor across all cases. Surface-averaged values are consistently higher than volume-averaged values, as the latter includes regions with zero infection risk and atmospheric CO_2 levels, lowering overall averages.

Notably, high CO_2 concentration does not imply high infection risk, as CO_2 is exhaled by all occupants, while infectious particles originate from an infector. Infection risk varies with infector position and airflow direction, whereas CO_2 distribution remains unaffected.

Elsarraj et al. [20] trained an Optimised Random Forest (ORF) model using volume-averaged POI and CO_2 concentration, incorporating ventilation rate to distinguish CO_2 thresholds across occupancy levels. However, assuming a single infector led to overlapping CO_2 values for the same POI, affecting model accuracy.

Analysing all surface and volume-averaged data was impractical due to overlapping CO_2 values at a given ventilation rate, which obscures clear trends.

Instead, heatmaps (Figures 5 & 6) were used to identify high-risk zones based on elevated infection probability. For these zones, only surface-averaged POI and CO_2 concentrations were extracted to provide a conservative representation of worst-case exposure conditions.

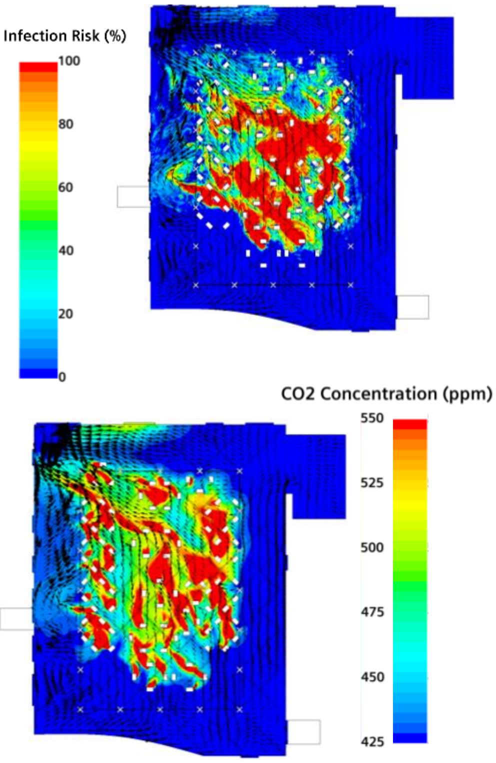

Figure 3. Contour and vector plots of the POI and the CO_2 concentration along the horizontal plane at a height of 1.2 m above the floor

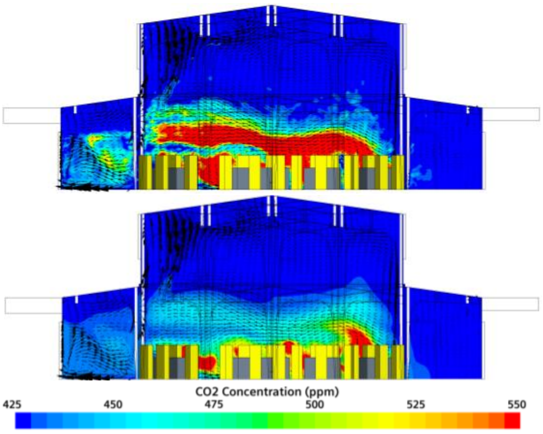

Figure 4. Contour and vector plots of the POI and the CO_2 concentration along the vertical mid-span plane.

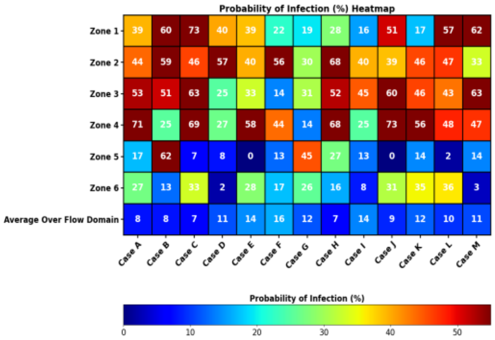

	Case A	Case B	Case C	Case D	Case E	Case F	Case G	Case H	Case I	Case J	Case K	Case L	Case M
Zone 1	39	60	73	40	39	22	19	28	16	51	17	57	62
Zone 2	44	59	46	57	40	56	30	68	40	39	46	47	33
Zone 3	53	51	63	25	33	14	31	52	45	60	46	43	63
Zone 4	71	25	69	27	58	44	14	68	25	73	56	48	47
Zone 5	17	62	7	8	0	13	45	27	13	0	14	2	14
Zone 6	27	13	33	2	28	17	26	16	8	31	35	36	3
Average Over Flow Domain	8	8	7	11	14	16	12	7	14	9	12	10	11

Figure 5. POI heatmaps for all cases for each zone.

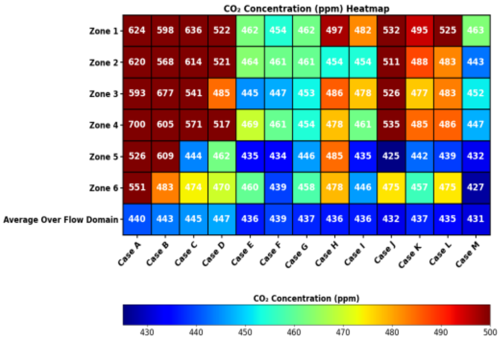

	Case A	Case B	Case C	Case D	Case E	Case F	Case G	Case H	Case I	Case J	Case K	Case L	Case M
Zone 1	624	598	636	522	462	454	462	497	482	532	495	525	463
Zone 2	620	568	614	521	464	461	461	454	454	511	488	483	443
Zone 3	593	677	541	485	445	447	453	486	478	526	477	483	452
Zone 4	700	605	571	517	469	461	454	478	461	535	485	486	447
Zone 5	526	609	444	462	435	434	446	485	435	425	442	439	432
Zone 6	551	483	474	470	460	439	458	478	446	475	457	475	427
Average Over Flow Domain	440	443	445	447	436	439	437	436	436	432	437	435	431

Figure 6. CO_2 concentration heatmaps for all cases for each zone.

4. Conclusion

This study developed a CFD-based framework for evaluating infection risk in a UK hospice using a Probability of Infection (POI) metric derived from an Eulerian-Lagrangian (E-L) model. The results demonstrate that CO_2 distribution, while often used as a ventilation performance indicator, differs significantly from the spatial behaviour of infectious aerosols, primarily due to diffusion effects absent in the POI formulation. This discrepancy validates the need for direct particle-based modelling when assessing airborne infection risk.

Heatmap analysis across multiple cases identified high-risk zones, revealing that infection risk is highly sensitive to infector position and airflow dynamics, rather than CO_2 concentration alone. These insights demonstrate the limitations of relying on CO_2 as a surrogate for exposure and highlight the value of spatially resolved CFD models in guiding ventilation strategies.

By quantifying infection risk based on clinically informed exposure metrics and airflow behaviour, this approach offers a robust tool for assessing and improving ventilation effectiveness in sensitive healthcare settings. The framework may be extended to other high-risk environments, such as care homes or waiting areas, to support evidence-based infection control strategies in post-pandemic building design.

REFERENCES

[1] J. Lu, J. Gu, J. Gu, K. Li, C. Xu, W. Su, Z. Lai, D. Zhou, C. Yu, B. Xu, Z. Yang, COVID-19 Outbreak Associated with Air Conditioning in Restaurant, Guangzhou, China, 2020, Emerg. Infect. Dis. 26 (2020) 1628–1631. https://doi.org/10.3201/eid2607.200764.

[2] L. Morawska, D.K. Milton, It Is Time to Address Airborne Transmission of Coronavirus Disease 2019 (COVID-19), Clin. Infect. Dis. 71 (2020) 2311–2313. https://doi.org/10.1093/CID/CIAA939.

[3] V. Stadnytskyi, C.E. Bax, A. Bax, P. Anfinrud, The airborne lifetime of small speech droplets and their potential importance in SARS-CoV-2 transmission, Proc. Natl. Acad. Sci. U. S. A. 117 (2020) 11875–11877. https://doi.org/10.1073/PNAS.2006874117/ASSET/03A58387-760C-4C37-9D6A-BB2FEF5BC447/ASSETS/GRAPHIC/PNAS.2006874117FIG01.JPEG.

[4] R. Zhang, Y. Li, A.L. Zhang, Y. Wang, M.J. Molina, Identifying airborne transmission as the dominant route for the spread of COVID-19, Proc. Natl. Acad. Sci. U. S. A. 117 (2020) 14857–14863. https://doi.org/10.1073/pnas.2009637117.

[5] Q.J. Leclerc, N.M. Fuller, L.E. Knight, S. Funk, G.M. Knight, What settings have been linked to SARS-CoV-2 transmission clusters?, Wellcome Open Res. 5 (2020). https://doi.org/10.12688/WELLCOMEOPENRES.15889.2.

[6] CIBSE, COVID-19 Ventilation Guidance, (2021) 1–26. https://www.cibse.org/knowledge-research/knowledge-portal/covid-19-guidance-ventilation-v4.

[7] ANSI/ASHRAE, ANSI/ASHRAE standard 62.1-2022:, Vent. Accept. Indoor Air Qual. Atlanta, GA, USA Am. Soc. Heating, Refrig. Airconditioning Eng. (2022).

[8] REHVA, REHVA COVID-19 guidance document version 4.1. How to operate HVAC and other buildings service systems to prevent the spread of the coronavirus (SARS-CoV-2) disease (COVID-19) in workplaces, 2021. https://www.rehva.eu/fileadmin/user_upload/REHVA_COVID-19_guidance_document_V4.1_15042021.pdf (accessed June 14, 2023).

[9] G. Pei, M. Taylor, D. Rim, Human exposure to respiratory aerosols in a ventilated room: Effects of ventilation condition, emission mode, and social distancing, Sustain. Cities Soc. 73 (2021).

https://doi.org/10.1016/j.scs.2021.103090.

[10] G.K. Rencken, E.K. Rutherford, N. Ghanta, J. Kongoletos, L. Glicksman, Patterns of SARS-CoV-2 aerosol spread in typical classrooms, Build. Environ. 204 (2021). https://doi.org/10.1016/j.buildenv.2021.108167.

[11] C. Ren, S.J. Cao, F. Haghighat, A practical approach for preventing dispersion of infection disease in naturally ventilated room, J. Build. Eng. 48 (2022) 103921. https://doi.org/10.1016/j.jobe.2021.103921.

[12] Q. Cao, M. Liu, X. Li, C.H. Lin, D. Wei, S. Ji, T. (Tim) Zhang, Q. Chen, Influencing factors in the simulation of airflow and particle transportation in aircraft cabins by CFD, Build. Environ. 207 (2022). https://doi.org/10.1016/j.buildenv.2021.108413.

[13] Y. Yan, X. Li, Y. Shang, J. Tu, Evaluation of airborne disease infection risks in an airliner cabin using the Lagrangian-based Wells-Riley approach, Build. Environ. 121 (2017) 79–92. https://doi.org/10.1016/J.BUILDENV.2017.05.013.

[14] Z. Liu, W. Zhuang, X. Hu, Z. Zhao, R. Rong, J. Li, N. Li, W. Ding, Potential infection risk assessment of improper bioaerosol experiment operation in one BSL-3 laboratory based on the improved Wells-Riley method, Build. Environ. 201 (2021) 107974. https://doi.org/10.1016/J.BUILDENV.2021.107974.

[15] B. Bake, P. Larsson, G. Ljungkvist, E. Ljungström, A.C. Olin, Exhaled particles and small airways, Respir. Res. 20 (2019). https://doi.org/10.1186/S12931-019-0970-9.

[16] C.T. Crowe, J.D. Schwarzkopf, M. Sommerfeld, Y. Tsuji, Multiphase flows with droplets and particles: Second edition, 2011.

[17] A. Keshmiri, M.A. Cotton, Y. Addad, D. Laurence, A. Keshmiri, M.A. Cotton, Y. Addad, · D Laurence, Turbulence Models and Large Eddy Simulations Applied to Ascending Mixed Convection Flows, Flow Turbul. Combust. 89 (2012) 407–434. https://doi.org/10.1007/s10494-012-9401-4.

[18] A. Keshmiri, A. Revell, H.G. Darabkhani, Assessment of a common nonlinear eddy-viscosity turbulence model in capturing laminarization in mixed convection flows, Numer. Heat Transf. Part A Appl. 69 (2016) 146–165. https://doi.org/10.1080/10407782.2015.1069672.

[19] A. Keshmiri, K. Osman, S. Benhamadouche, N. Shokri, Assessment of advanced RANS models against large eddy simulation and experimental data in the investigation of ribbed passages with passive heat transfer, Numer. Heat Transf. Part B Fundam. 69 (2016) 96–110. https://doi.org/10.1080/10407790.2015.1096641.

[20] M. Elsarraj, Y. Mahmoudi, A. Keshmiri, Quantifying indoor infection risk based on a metric-driven approach and machine learning, Build. Environ. 251 (2024) 111225. https://doi.org/10.1016/J.BUILDENV.2024.111225.

[21] L. Schiller, Über die grundlegenden Berechnungen bei der Schwerkraftaufbereitung, Z. Vereines Dtsch. Inge. 77 (1933) 318–321.

[22] W.F. Wells, Airborne contagion and air hygiene: an ecological study of droplet infections, J. Am. Med. Assoc. 159 (1955) 90. https://jamanetwork.com/journals/jama/article-abstract/302159.

[23] E.C. Riley, G. Murphy, R.L. Riley, Airborne spread of measles in a suburban elementary school, Am. J. Epidemiol. 107 (1978) 421–432. https://doi.org/10.1093/oxfordjournals.aje.a112560.

[24] R. Wölfel, V.M. Corman, W. Guggemos, M. Seilmaier, S. Zange, M.A. Müller, D. Niemeyer, T.C. Jones, P. Vollmar, C. Rothe, M. Hoelscher, T. Bleicker, S. Brünink, J. Schneider, R. Ehmann, K. Zwirglmaier, C. Drosten, C. Wendtner, Virological assessment of hospitalized patients with COVID-2019, Nat. 2020 5817809. 581 (2020) 465–469. https://doi.org/10.1038/s41586-020-2196-x.

[25] X. Li, D. Lester, G. Rosengarten, C. Aboltins, M. Patel, I. Cole, A spatiotemporally resolved infection risk model for airborne transmission of COVID-19 variants in indoor spaces, Sci. Total Environ. 812 (2022) 152592. https://doi.org/10.1016/j.scitotenv.2021.152592.

[26] C.Y.H. Chao, M.P. Wan, L. Morawska, G.R. Johnson, Z.D. Ristovski, M. Hargreaves, K. Mengersen, S. Corbett, Y. Li, X. Xie, D. Katoshevski, Characterization of expiration air jets and droplet size distributions immediately at the mouth opening, J. Aerosol Sci. 40 (2009) 122–133. https://doi.org/10.1016/j.jaerosci.2008.10.003.

[27] X. Li, Y. Shang, Y. Yan, L. Yang, J. Tu, Modelling of evaporation of cough droplets in inhomogeneous humidity fields using the

multi-component Eulerian-Lagrangian approach, Build. Environ. 128 (2018) 68–76. https://doi.org/10.1016/j.buildenv.2017.11.025.

[28] V. Stadnytskyi, C.E. Bax, A. Bax, P. Anfinrud, The airborne lifetime of small speech droplets and their potential importance in SARS-CoV-2 transmission, Proc. Natl. Acad. Sci. U. S. A. 117 (2020) 11875–11877. https://doi.org/10.1073/pnas.2006874117.

[29] D.K. Milton, M.P. Fabian, B.J. Cowling, M.L. Grantham, J.J. Mcdevitt, Influenza Virus Aerosols in Human Exhaled Breath: Particle Size, Culturability, and Effect of Surgical Masks, PLoS Pathog. 9 (2013) 1003205. https://doi.org/10.1371/journal.ppat.1003205.

[30] M. Sandberg, What is ventilation efficiency?, Build. Environ. 16 (1981) 123–135. https://doi.org/10.1016/0360-1323(81)90028-7.

[31] L. Tian, Z. Lin, Q. Wang, Comparison of gaseous contaminant diffusion under stratum ventilation and under displacement ventilation, Build. Environ. 45 (2010) 2035–2046. https://doi.org/10.1016/J.BUILDENV.2010.01.002.

[32] ANSI/ASHRAE, ANSI/ASHRAE standard 62.1-2013:, Vent. Accept. Indoor Air Qual. Atlanta, GA, USA Am. Soc. Heating, Refrig. Airconditioning Eng. (2013). www.ashrae.org/technology.

[33] M. Sandberg, M. Sjöberg, The use of moments for assessing air quality in ventilated rooms, Build. Environ. 18 (1983) 181–197. https://doi.org/10.1016/0360-1323(83)90026-4.

[34] American Society of Heating Refrigerating and Air-Conditioning Engineers (ASHRAE), ASHRAE handbook: Fundamentals, American Society of Heating, Refrigeration and Air-Conditioning Engineers, 2009.

[35] I.E.S. Limited., SOFTWARE VALIDATION AND APPROVAL, (2014). https://www.iesve.com/software/software-validation?utm_source=chatgpt.com (accessed November 27, 2024).

[36] CIBSE, Applications Manual AM 11 - Building performance modelling, 2015. https://www.cibse.org/knowledge-research/knowledge-portal/applications-manual-11-building-performance-modelling-2015?utm_source=chatgpt.com (accessed November 27, 2024).

[37] M. Elsarraj, Y. Mahmoudi, A. Keshmiri, Linking airflow dynamics to infection risk reduction and predictive strategies, J. Build. Eng. 110 (2025) 113027. https://doi.org/10.1016/J.JOBE.2025.113027.

[38] S.B. Kwon, J. Park, J. Jang, Y. Cho, D.S. Park, C. Kim, G.N. Bae, A. Jang, Study on the initial velocity distribution of exhaled air from coughing and speaking, Chemosphere. 87 (2012) 1260–1264. https://doi.org/10.1016/j.chemosphere.2012.01.032.

[39] Z.T. Ai, A.K. Melikov, Airborne spread of expiratory droplet nuclei between the occupants of indoor environments: A review, Indoor Air. 28 (2018) 500–524. https://doi.org/10.1111/ina.12465.

[40] A.C.K. Lai, W.W. Nazaroff, Modeling indoor particle deposition from turbulent flow onto smooth surfaces, J. Aerosol Sci. 31 (2000) 463–476. https://doi.org/10.1016/S0021-8502(99)00536-4.